Full-Speed Range Control of a Symmetrical Six-Phase Automotive IPMSM Drive with a Cascaded DC-link Configuration

Full-Speed Range Control of a Symmetrical Six-Phase Automotive IPMSM Drive with a Cascaded DC-link Configuration

Andres Sierra-Gonzalez, Paolo Pescetto, Fernando Alvarez-Gonzalez, Borja Heriz, Elena Trancho, Hannes Lacher, Edorta Ibarra, Gianmario Pellegrino

***Abstract*—This work considers the utilization of a symmetrical six-phase interior permanent magnet synchronous machine drive, including a cascaded dc-link configuration, to make up an electric vehicle propulsion system. This way, fast charging capabilities are provided while avoiding the utilization of power semiconductors with high voltage ratings. In this scenario, the control algorithm must deal with the non-linearities of the machine, providing an accurate setpoint command for the whole torque and speed range of the drive. Therefore, cross-coupling effects between the winding sets must be considered, and the voltage of the cascaded dc-link capacitors must be actively monitored and balanced. In view of this, the authors propose a novel control approach that provides all these functionalities. The proposal is experimentally validated in a full-scale 70 kW electric drive prototype, tested in a laboratory set-up and in an electric vehicle under real driving cycle conditions.**

***Index Terms*—symmetrical six-phase, dual three-phase, IPMSM, full-speed range control, cascaded dc-link, multiphase, field weakening, electric vehicles, dc-voltage balancing, driving cycle.**

I. Introduction

Transport electrification plays a relevant role in the mitigation of global warming [1]–[3]. Therefore, many resources are being invested in the development of new technologies. For example, from 2014 to 2020, the European Union has invested 3.07 billion euros in transport electrification research projects [4]. One key investigation area is the development of new electric drivetrains that would improve the efficiency, driving range, and performance of next-generation Electric Vehicles (EV).

This research has received funding from the European Union's Horizon 2020 research and innovation programme under project FITGEN, grant agreement No 824335. This work was supported in part by the Government of the Basque Country within the fund for research groups of the Basque University system IT1440-22 and by the MCIN/AEI/10.13039/501100011033 within the project PID2020-115126RB-I00, by the Government of the Basque Country within the research program ELKARTEK as the projects PROH2BIO (KK-2022/00051) and VEGAN (KK-2021/00044).

A. Sierra-Gonzalez, F. Alvarez-Gonzalez, B. Heriz, and E. Trancho are with TECNALIA, Basque Research and Technology Alliance (BRTA), 48160, Derio, Spain (e-mail: andres.sierra@tecnalia.com; fernando.alvarez@tecnalia.com; borja.heriz@tecnalia.com; elena.trancho@tecnalia.com).

P. Pescetto, and G. Pellegrino are with the Department of Energy Galileo Ferraris, Politecnico di Torino, 10129 Torino, Italy (e-mail: paolo.pescetto@polito.it; gianmario.pellegrino@polito.it).

E. Ibarra is with the Department of Electronics Technology, University of the Basque Country (UPV/EHU), 48013, Bilbao, Spain (e-mail: edorta.ibarra@ehu.eus).

H. Lacher is with the Mobility Department, Austrian Institute of Technology GmbH, 1210, Vienna, Austria (e-mail:hannes.lacher@ait.ac.at).

Electrical propulsion systems powered by multiphase drives are gaining attention over conventional three-phase solutions thanks to their advantages, such as power splitting, increased power density, better efficiency, lower current rating power electronics components, lower torque pulsations, additional degrees of freedom in the control, and higher fault tolerance [5], [6]. Among all the available multiphase architectures, dual three-phase or six-phase Permanent Magnet Synchronous Machine (PMSM) drives are being considered for the near future EV applications, as the technological transition from three-phase systems is relatively straightforward [7], [8].

In this context, the European Union-funded project FITGEN aims to develop a functionally integrated e-axle ready to be implemented in third-generation electric vehicles [9]. This project's key performance indicators regarding the state of the art of EV powertrain at the project's start are [10]:

- a 40 % increase in the power density of the electric machine, with a rotational speed up to 22500 rpm.
- a 50 % increase in the power density of the inverter, thanks to the adoption of SiC components.
- an affordable super-fast charging capability (120 kW peak) thanks to the dc/dc converter and up to 11 kW domestic charging through innovative on-board charger topologies.
- an increase in the EV driving range from 740 to 1050 km (including 75 minutes of charging time) in real-world free-way driving.

To achieve these targets, the e-axle incorporates a symmetrical six-phase Interior Permanent Magnet Synchronous Machine (IPMSM) with two isolated neutral points, driven by a full-SiC inverter with a switching frequency of up to 24 kHz. This propulsion system also includes a dc/dc converter mounted between the battery and power inverter (Fig. 1). The incorporation of the dc/dc converter increases the amount of power electronics elements that can produce additional conduction and switching losses and also increases cost. However, the dc-link voltage can be adapted in real-time through a dedicated control strategy. This way, overall system power losses (converters and electric machine) can be minimized, compensating to a great extent the impact of the additional elements over efficiency [11]–[14].

Thanks to the aforementioned hardware configuration, the following advantages can be obtained [12], [15]–[19]: (a) The dc-link is boosted to the 800 V range from a 320 V battery pack to provide embedded super-fast charging capabilities,

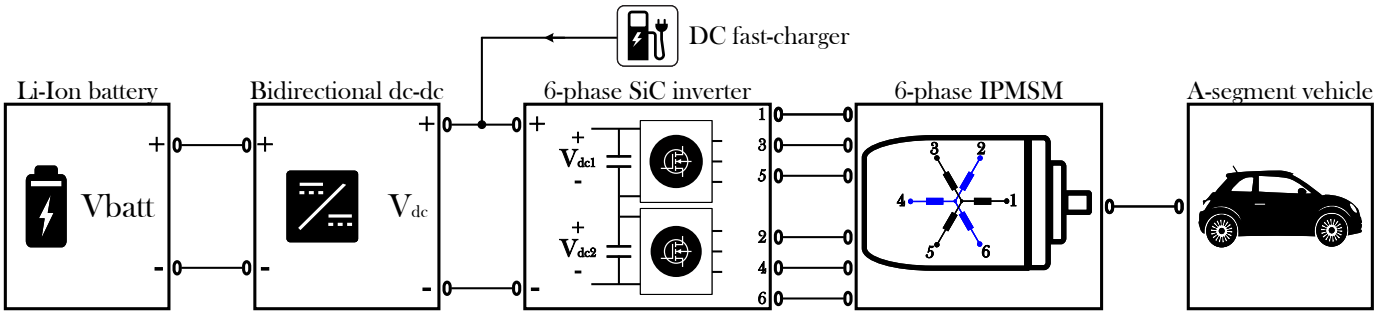

Figure 1: General diagram of the FITGEN e-axle including a dc/dc converter, a six-phase SiC-based inverter with a cascaded dc-link capacitor configuration and a dual three-phase IPMSM.

$$\begin{bmatrix} i_{D1} \\ i_{Q1} \\ i_{D2} \\ i_{Q2} \\ i_{H1} \\ i_{H2} \end{bmatrix} = \frac{1}{3} \begin{bmatrix} cos(\theta_e) & cos(\theta_e - \alpha) & cos(\theta_e - 2\alpha) & \dots & cos(\theta_e - 5\alpha) \\ -sin(\theta_e) & -sin(\theta_e - \alpha) & -sin(\theta_e - 2\alpha) & \dots & -sin(\theta_e - 5\alpha) \\ cos(5\theta_e) & cos(5\theta_e - 2\alpha) & cos(5\theta_e - 4\alpha) & \dots & cos(5\theta_e - 10\alpha) \\ -sin(5\theta_e) & -sin(5\theta_e - 2\alpha) & -sin(5\theta_e - 4\alpha) & \dots & -sin(5\theta_e - 10\alpha) \\ 1 & 0 & 1 & \dots & 0 \\ 0 & 1 & 0 & \dots & 1 \end{bmatrix} \begin{bmatrix} i_1 \\ i_2 \\ i_3 \\ i_4 \\ i_5 \\ i_6 \end{bmatrix}, \ \alpha = \frac{\pi}{3}. \tag{1}$$

(b) a lower current ripple and a higher power factor can be obtained, and (c) the dc-link voltage can be regulated regardless the State of Charge (SoC) of the battery pack.

To avoid the utilization of power semiconductors with high voltage ratings, which exhibit higher conduction losses and cost, a cascaded dc-link configuration has been defined within project FITGEN. This configuration consists of two three-phase inverter units connected in series, where each unit feeds one of the motor winding sets (Fig. 1).

Considering all the above, the electric machine control system must deal with the following aspects:

1) *Optimal operation*: the controller must compute minimum magnitude current references according to an operating point in the full speed range [Maximum Torque per Ampere (MTPA) and field weakening (FW) operation]. This computation must consider the non-linear and highly coupled nature of the automotive IPMSM to guarantee accurate torque control.
2) *Current regulation*: the control algorithm must properly regulate the stator currents and generate the firing pulses of the power semiconductors.
3) *Active dc-link voltage balancing*: because of the dc-link cascaded configuration, an algorithm must be incorporated to balance the input voltage of each three-phase converter unit.

The first two aspects have been extensively studied in the scientific literature for three-phase systems. For example, if a convenient modeling approach is chosen, techniques for calculating the optimal current trajectories of a three-phase machine [20], [21] can be easily adapted for the six-phase scenario. In this manuscript, the authors re-adapt their previously proposed setpoint generation approach for three-phase systems [22]. For current regulation, the well-known Field Oriented Control (FOC) approach has been followed.

Regarding the active dc-link voltage balancing, this kind of cascaded configuration (and their corresponding voltage balancing controllers) has been previously proposed in the literature for applications such as wind turbines based on asymmetrical six-phase induction machines [23], twelve-phase induction machines [24], twelve-phase surface mounted permanent magnet synchronous generators [25] and nine three-phase decoupled-segment generators [26]. However, these applications only consider the generating operation when the dc-voltage of each inverter unit is asymptotically stable, even in open-loop. On the other hand, in [27] and [28], a cascaded configuration is theoretically proposed for EV powertrains. Therefore, motoring operation is considered. In this scenario, a close-loop balancing algorithm is required due to unstable behavior of the dc-link voltages during traction operation.

Considering all the previous, the main contributions of this work can be summarized as follows:

- A novel dc-link balancing algorithm for cascaded inverter configurations is proposed. At the best of the authors' knowledge, the cascaded topology has never been previously used in full-scale traction IPMSMs. Such application introduces relevant control challenges related to the EVs requirements, such as fast control dynamic, extended speed range including MTPA and FW operation, bidirectional power flow, non-linear magnetic saturation, cross-couplings, and relevant switching frequency operation.
- A combined utilization of two vector representations within the same controller, i.e., the "multiphase" and "double three-phase" representations, is proposed to take advantage of both.
- The solution is verified at TRL7 in a real electric vehicle comprising an automotive 70 kW six-phase IPMSM drive and under real driving conditions. This way, the industrial applicability of the proposal is fully demonstrated, which can be of great interest to industrial engineers, researchers, OEMs, and vehicle manufacturers alike.

This paper follows the conference version presented in [1]. Apart from including experimental verification, in this article,

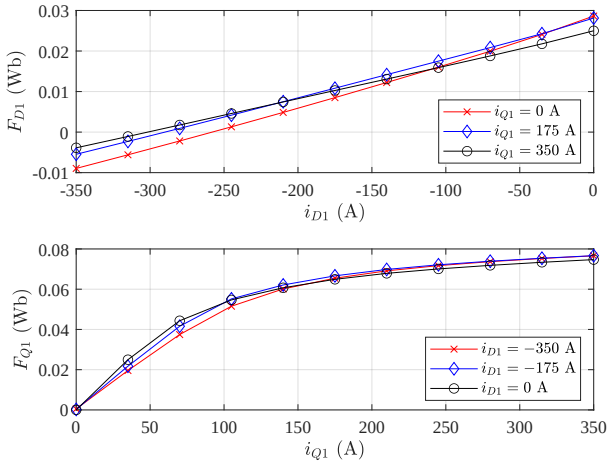

Figure 2: Dual three-phase IPMSM fluxes in the $D1-Q1$ reference frame.

such preliminary work is extended, i.e., a mathematical model of the cascaded dc-link is introduced, the procedure to determine the optimum current setpoint trajectories is explained, and the voltage balancing algorithm is optimized and extended for regenerative braking operation. The modulation approach is also highlighted: an interleaved PWM scheme is implemented to cancel the high current ripple caused by the motor winding distribution.

II. Mathematical Model of the System

A. Symmetrical dual three-phase IPMSM

As the proposed controller combines two vector representations, herein named "multiphase" ($\mathbf{T_1}$ matrix) and "double three-phase" ($\mathbf{T_2}$ matrix), both are mathematically described.

The six-phase Clarke-Park transformation matrix $\mathbf{T_1}$, defined in (1), transforms the phase currents, voltages, and flux linkages of the symmetrical IPMSM into the D_1-Q_1 (fundamental harmonics) and D_2-Q_2 (5th and 7th harmonics) planes, resulting in the following set of equations [29]:

$$\begin{cases} v_{D1} = R_s i_{D1} + L_{D1}\frac{\mathrm{d}i_{D1}}{\mathrm{d}t} - \omega_e L_{Q1} i_{Q1} \\ v_{Q1} = R_s i_{Q1} + L_{Q1}\frac{\mathrm{d}i_{Q1}}{\mathrm{d}t} + \omega_e (L_{D1} i_{D1} + \psi_{PM1}) \end{cases} \quad (2)$$

$$\begin{cases} v_{D2} = R_s i_{D2} + L_{D2}\frac{\mathrm{d}i_{D2}}{\mathrm{d}t} - 5\omega_e L_{Q2} i_{Q2} \\ v_{Q2} = R_s i_{Q2} + L_{Q2}\frac{\mathrm{d}i_{Q2}}{\mathrm{d}t} + 5\omega_e (L_{D2} i_{D2} + \psi_{PM5}) \end{cases} \quad (3)$$

$$T_{em} = 3N_p \left[\psi_{PM} i_{Q1} + (L_{D1} - L_{Q1}) i_{D1} i_{Q1}\right], \quad (4)$$

where v_{DQ}, i_{DQ}, L_{DQ} and ψ_{PM} are the stator voltages, currents, inductances, and permanent magnet fluxes represented in the D_1-Q_1 and D_2-Q_2 synchronous frames, R_s is the stator resistance, N_p is the pole-pair number and $\omega_e = N_p \omega_{mech}$ is the electrical speed. Herein, non-linear magnetic saturation is considered by adopting current-dependent fluxes and inductances. Fig. 2 shows the fluxes of the automotive electric machine under test, computed using a Finite Element Model (FEM).

In this vector representation, the two planes are decoupled. From (4), it is deduced that torque can be controlled by only regulating the D_1-Q_1 plane currents. Therefore, the optimal current references are easier to calculate, with the advantage that cross-coupling between the two three-phase sets is considered [1].

Note that plane decoupling is not possible when the well-known Clarke-Park three-phase transformation, here called $\mathbf{T_2}$, is applied to each three-phase set [1], [29]. However, this vector transformation facilitates the independent regulation of the power consumed (or delivered during regenerative braking) by each three-phase set. The application of $\mathbf{T_2}$ on the machine equations results in:

$$\begin{cases} v_{d1} = & R_s i_{d1} + L_d\frac{\mathrm{d}i_{d1}}{\mathrm{d}t} - \omega_e L_q i_{q1} + M_d\frac{\mathrm{d}i_{d2}}{\mathrm{d}t} - \omega_e M_q i_{q2} \\ v_{q1} = & R_s i_{q1} + L_q\frac{\mathrm{d}i_{q1}}{\mathrm{d}t} + \omega_e L_d i_{d1} + M_q\frac{\mathrm{d}i_{q2}}{\mathrm{d}t} + \omega_e M_d i_{d2} \\ & + \omega_e \psi_{PM} \end{cases} \quad (5)$$

$$\begin{cases} v_{d2} = & R_s i_{d2} + L_d\frac{\mathrm{d}i_{d2}}{\mathrm{d}t} - \omega_e L_q i_{q2} + M_d\frac{\mathrm{d}i_{d1}}{\mathrm{d}t} - \omega_e M_q i_{q1} \\ v_{q2} = & R_s i_{q2} + L_q\frac{\mathrm{d}i_{q2}}{\mathrm{d}t} + \omega_e L_d i_{d2} + M_q\frac{\mathrm{d}i_{q1}}{\mathrm{d}t} + \omega_e M_d i_{d1} \\ & + \omega_e \psi_{PM} \end{cases} \quad (6)$$

$$T_{em} = \frac{3}{2} N_p [\psi_{PM}(i_{q1} + i_{q2}) + (L_d - L_q)(i_{d1} i_{q1} + i_{d2} i_{q2}) + (M_d - M_q)(i_{d1} i_{q2} + i_{d2} i_{q1})], \quad (7)$$

where v_{dq}, i_{dq} and ψ_{PM} are the stator voltages, phase currents, and permanent magnet fluxes represented in the d_1-q_1 and d_2-q_2 synchronous frames. Meanwhile, the terms L_{dq} and M_{dq} are derived by applying $\mathbf{T_2}$ to the matrix of mutual- and self-inductances of the stator.

The control approach proposed in this paper takes advantage of both vector representations.

B. Mathematical description of the cascaded dc-link

The controller utilizes the q-axis currents to balance the dc voltages (See section III-B). Considering this, the description of how the voltages behave when the q-axis currents change is presented below. Fig. 3 shows the dc-link circuit of the cascaded configuration, where i_{dc} is the current circulating from/to the dc/dc converter, V_{dcj} is the voltage of capacitor C_j, $i_{in,j}$ is the input current to the inverter unit j, and i_{Cj} is the current flowing through capacitor C_j ($j \in \{1,2\}$). Using the Kirchhoff laws, the voltage on each dc-link capacitor is:

$$V_{dcj} = \frac{1}{C_j}\int (i_{dc} - i_{inj}) dt. \quad (8)$$

In order to analytically determine the relationship between the dc-link voltages and the electric machine input currents, the expression of the average inverter's input currents is considered [30], [31]:

$$avg(i_{inj}) = \frac{3}{4} |\vec{i}_{dqj}| m_j cos\phi_j, \quad (9)$$

where $|\vec{i}_{dqj}|$ is the current vector magnitude of the j-th three-phase set represented in the dq reference frame, m_j is the modulation index and $cos\phi_j$ is the power factor. By combining

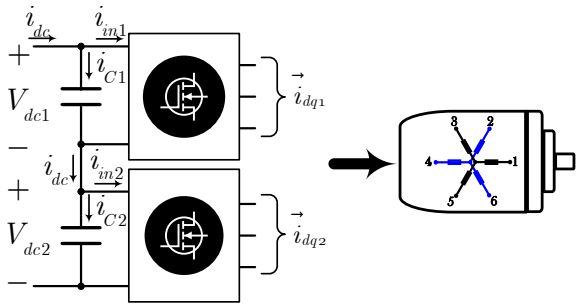

Figure 3: Currents circulating through the cascaded dc-link configuration.

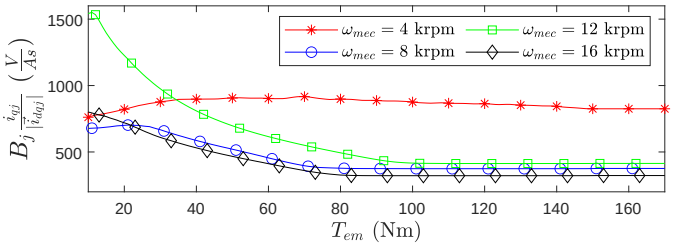

Figure 4: $B_j i_{qj}/|\vec{i}_{dqj}|$ vs. T_{em} for various values of ω_{mec}, capacitors C_1=C_2=320 μF, and with a total dc voltage of 700 V.

(8) and (9), it is possible to determine the voltage variation in V_{dcj} due to a change in the current magnitude $|\vec{i}_{dqj}|$:

$$\Delta V_{dcj} = -\int B_j \Delta|\vec{i}_{dqj}|dt, \tag{10}$$

where $B_j = 3m_j cos\phi_j/4C_j$.

If the variations in the magnitude ($\Delta|\vec{i}_{dqj}|$) are due to changes in the current component i_{qj}, then

$$\Delta|\vec{i}_{dqj}| = \sqrt{i_{dj}^2 + (i_{qj} + \Delta i_{qj})^2} - \sqrt{i_{dj}^2 + i_{qj}^2}. \tag{11}$$

Multiplying and dividing (11) by the term χ:

$$\chi = \sqrt{i_{dj}^2 + (i_{qj} + \Delta i_{qj})^2} + \sqrt{i_{dj}^2 + i_{qj}^2}, \tag{12}$$

the following approximation holds true as long as $|\Delta i_{qj}| \ll |\vec{i}_{dqj}|$:

$$\Delta|\vec{i}_{dqj}| \approx \frac{i_{qj}}{|\vec{i}_{dqj}|}\Delta i_{qj}. \tag{13}$$

Substituting (13) into (10) shows that a change in the q-axis current (Δi_{qj}) will generate the following variation in V_{dcj}:

$$\Delta V_{dcj} \approx -\int B_j \frac{i_{qj}}{|\vec{i}_{dqj}|}\Delta i_{qj} dt. \tag{14}$$

From (8) to (14), the following considerations about the dynamic behavior of the cascaded capacitors can be drawn (identical three-phase windings and inverter units are considered):

- During steady state, $i_{in1} = i_{in2}$, $B_1 = B_2$, and $V_{dc1} = V_{dc2} = V_{dc}/2$. However, as pointed out in [23], [27], unless a voltage balancing strategy is included, even a slight unbalance in the system will cause dc-link voltages to diverge.
- V_{dc} is imposed by the dc/dc converter. As $V_{dc1}+V_{dc2} = V_{dc}$, then $\Delta V_{dc1} = -\Delta V_{dc2}$. From (8) and considering the circuit arrangement of Fig. 3, after an initial balancing, the voltage in both capacitors is:

$$V_{dc1} = \frac{1}{C_1 + C_2}\int (i_{in2} - i_{in1})\, dt + \frac{V_{dc}}{2}, \tag{15}$$

$$V_{dc2} = \frac{1}{C_1 + C_2}\int (i_{in1} - i_{in2})\, dt + \frac{V_{dc}}{2}. \tag{16}$$

Accordingly, permanent voltage unbalance is solely generated by an unbalanced power consumption of each three-phase inverter/machine unit.

- In motoring mode, an increase in the q-axis current's magnitude will cause a decrease in the associated dc-link voltage ($|i_{qj} + \Delta i_{qj}| > |i_{qj}|$ then $\Delta V_{dcj} < 0$).
- In contrast, in regenerative mode, if $|i_{qj} + \Delta i_{qj}| > |i_{qj}|$, then $\Delta V_{dcj} > 0$.
- Finally, Fig. 4 shows the variation of $B_j i_{qj}/|\vec{i}_{dqj}|$ with the operating point for the motor under test, retrieved through FEM data. From Fig. 4 and (14), the non-linear relationship between the q-axis current and dc-link voltage is clear.

III. Proposed Torque Control Algorithm with DC-Link Voltage Balancing Capabilities

Fig. 5 shows the general block diagram of the proposed *multiphase torque control* strategy. It aims to deliver the requested torque while keeping the cascaded dc-links balanced and the stator voltage below its maximum limit when operating above base speed. The controller is divided into three stages:

1) The first stage generates the optimal current setpoints considering the required torque and the actual state (speed, stator, and dc voltages) of the machine for the whole operation range (below and above base speed). Setpoints are obtained by means of $D-Q$ representation ($\mathbf{T_1}$) of the motor, as this representation is simpler and considers all the cross-couplings among phases and three-phase sets.
2) The second stage incorporates the active voltage balancing functionality. This stage is done in the $d-q$ space ($\mathbf{T_2}$) as the balancing requires varying the current of each three-phase set.
3) The third stage includes the synchronous current regulation loops, one per current loop, and the PWM technique.

A. Currents setpoint generation and field weakening control

For the generation of the optimal current setpoints, a simple solution with a relatively low computational burden is to pre-compute these references offline, storing them into Look-up tables (LUTs) [20]. This offline computation is done in the $D-Q$ frame, where the motor is considered as a unit, and both sets interact to produce the required torque. For flux-weakening operation, the current setpoint is speed dependent. Moreover, optimal current setpoints also depend on the dc-link voltage and rotor temperature, requiring, in principle, 4D LUTs. This increases the computational burden and the required memory storage. To avoid it, the measured speed is normalized with respect to the rated dc-link voltage (Fig. 6), as there is a linear

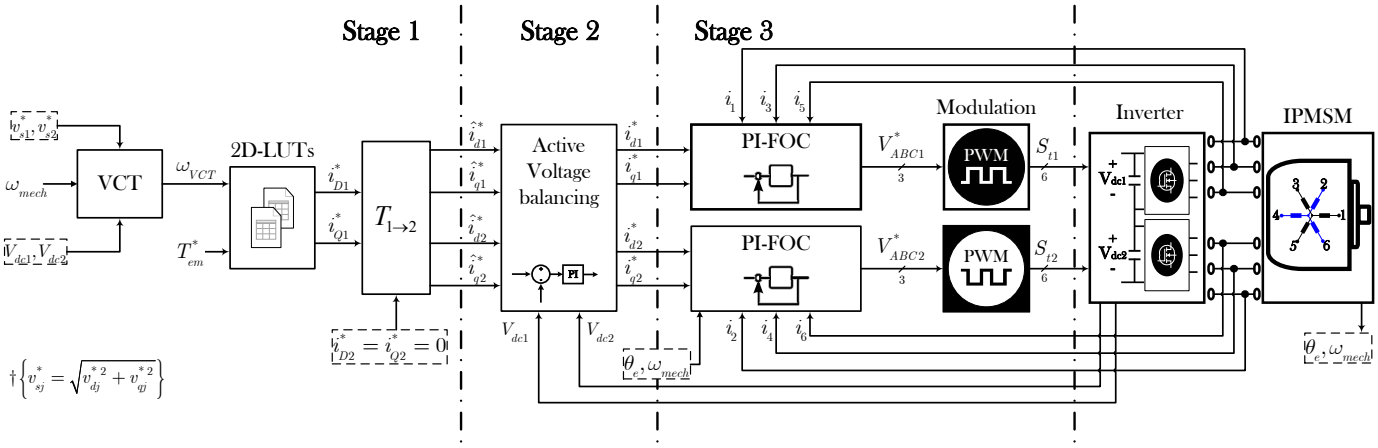

Figure 5: Block diagram of the proposed *multiphase* torque control.

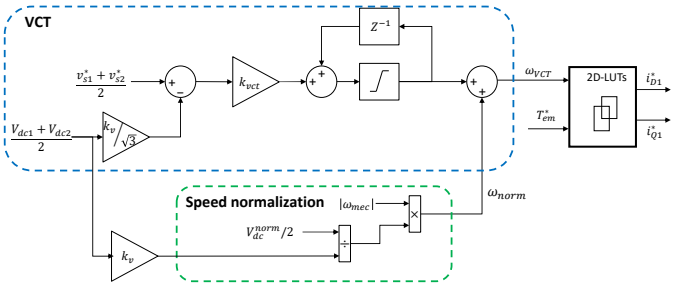

Figure 6: VCT and speed normalization blocks.

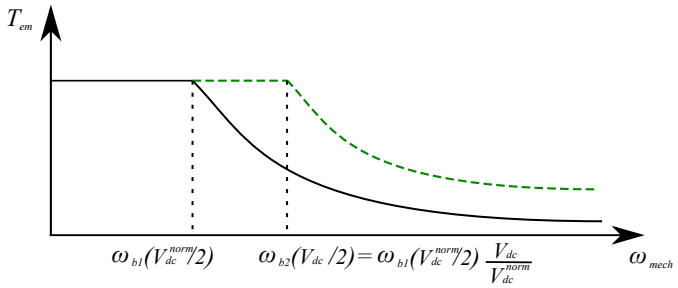

Figure 7: V_{dc} vs. torque-speed curve.

relationship between two torque-speed curves computed for different values of the dc-link voltage (Fig. 7).

With regard to rotor temperature, its measurement or estimation adds hardware or software complexity to the system. Consequently, it is of common practice in the industry not to consider such magnitude within the controller [32]. However, rotor temperature variations can produce deviations between the nominal and actual electrical parameters of the machine. In order to improve the robustness of the algorithm, a Voltage Constraint Tracking (VCT) feedback (Fig. 6) is utilized [22]. The aim of the VCT loop is to maintain the stator voltage vector close to the voltage limit margin during FW operation despite the appearance of significant parameter deviations that could jeopardize the system operation. To achieve this, the VCT varies the normalized speed fed to the LUTs depending on the error between the current control reference voltage v_s^* and the voltage limit. If PWM with triplen harmonics injection is implemented, the voltage limit is $k_v V_{dcj}/\sqrt{3}$, where k_v = 0.9 is used to provide a safe margin.

Thus, both the speed normalization and the incorporation of the VCT feedback loop permit the adoption of simpler 2D LUTs [22].

For the calculation of the 2-D LUTs, the model represented by (2), (3) and (4) is considered. Then, optimum currents are calculated by using the magnetic characteristic of the machine, either measured [33]–[35] or computed by FEM. Since i_{D1} and i_{Q1} are the ones in charge of producing torque, only two LUTs are needed. The computational steps followed are:

1) Using the FEM data and (4), the electromagnetic torque matrix is calculated for all i_{D1} and i_{Q1} combinations.
2) For each T_{em}^*, between $T_{min} = 0$ and T_{max}, the constant torque curve is computed, the MTPA point is found, and the base speed is calculated.
3) The Maximum Torque per Volt (MTPV) curve is computed. In this particular case, the MTPV curve is never reached considering the dc voltage range and the maximum mechanical speed of the drive under test.
4) The intersection points between the constant torque curves, the maximum current circle, and the MTPV curve are determined.
5) For each value of T_{em}^*, the curves are delimited to the desired ranges and concatenated to form the optimal current trajectories.
6) For each calculated point, its associated speed is computed and linked.
7) i_{D1} and i_{Q1} LUTs are sorted, sized, packed and saved.

The current trajectories calculated for the machine under test following these steps are shown in Fig. 8.

B. dc-link voltage balancing algorithm

Once the optimal setpoints $i_{D1}^* - i_{Q1}^*$ are calculated, they are transformed into the $d_1 - q_1$ and $d_2 - q_2$ planes. This is

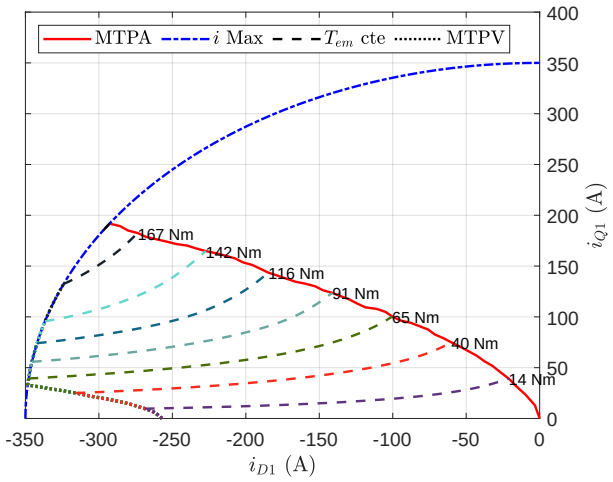

Figure 8: Current setpoint trajectories for the prototype under test.

done by applying the transformation $\mathbf{T_{1\to 2}} = \mathbf{T_2}\mathbf{T_1^{-1}}$:

$$\begin{bmatrix} d_1 \\ q_1 \\ h_1 \\ d_2 \\ q_2 \\ h_2 \end{bmatrix} = \begin{bmatrix} 1 & 0 & cos(6\theta_e) & -sin(4\theta_e) & 0 & 0 \\ 0 & 1 & -sin(6\theta_e) & cos(4\theta_e) & 0 & 0 \\ 0 & 0 & 0 & 0 & 1 & 0 \\ 1 & 0 & -cos(6\theta_e) & sin(6\theta_e) & 0 & 0 \\ 0 & 1 & sin(6\theta_e) & cos(6\theta_e) & 0 & 0 \\ 0 & 0 & 0 & 0 & 0 & 1 \end{bmatrix} \begin{bmatrix} D_1 \\ Q_1 \\ D_2 \\ Q_2 \\ H_1 \\ H_2 \end{bmatrix}. \tag{17}$$

As can be seen from (17), if D_2 and Q_2 are null then the components $d_1 = d_2 = D_1$ and $q_1 = q_2 = Q_1$.

Fig. 9 shows the block diagram of the proposed dc-link voltage balancing algorithm, which modifies the current references according to the error between the measured dc-link voltage of each set. For convenience and as it is sufficient to act over one reference current per three-phase set to modify their power delivery, it has been chosen to change only $\hat{i}^*_{q1}$ and $\hat{i}^*_{q2}$, avoiding to vary the flux-related current setpoints ($\hat{i}^*_{d1}$, $\hat{i}^*_{d2}$). A proportional-integral (PI) regulator computes the variations Δi_{q1} and Δi_{q2} required to balance the voltages. Then, q-axis references are modified as:

$$i^*_{qj} = (|\hat{i}^*_{qj}| - \Delta i_{qj}) sign(\hat{i}^*_{qj}). \tag{18}$$

The PI gains have been set through simulations and empirically fine-tuned in the experimental test bench. As stated previously, increasing or decreasing the magnitude of the reference currents must be set according to the sign of the machine power (P_M). Note that the machine is in motoring mode when $P_M > 0$ and in regenerative operation when $P_M < 0$.

Although theoretically only a proportional action is needed to achieve zero steady-state error (14), an integral action has been incorporated to compensate real machine phenomena such as manufacturing asymmetry, unbalance between three-phase assemblies, partial saturation, magnetic unbalances, or parasitic impedances. Automotive-grade components are used in this application. Thus, parametric dispersion of the components and their parasitic resistance is expected to be minor but still unavoidable. Therefore, the voltage balancing algorithm is necessary, and even at steady-state, one three-phase set

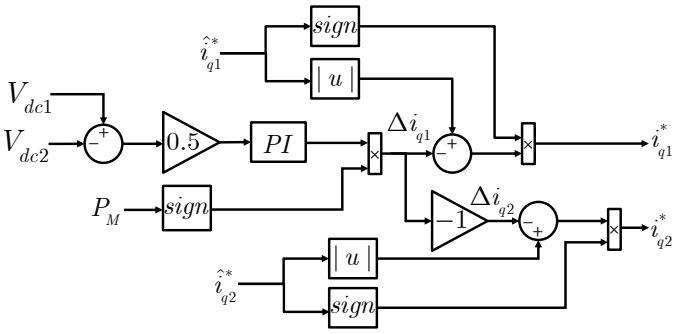

Figure 9: Block diagram of the proposed active voltage balancing algorithm.

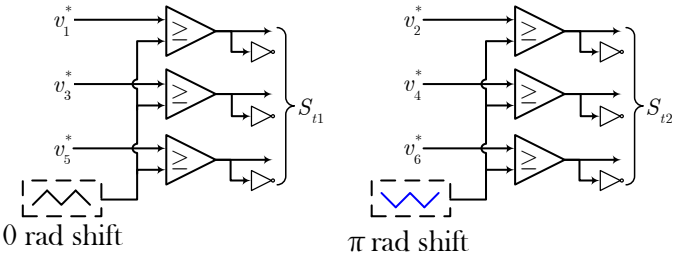

Figure 10: Implemented interleaved PWM strategy with a π radians phase-shift for the second winding set.

can drive more current than the other one, but the current discrepancy is expected to be minor and not significantly affect the losses or the lifetime of the drive.

C. Current regulation loops and adapted PWM scheme for symmetrical IPMSM with overlapped windings

The last stage of the six-phase torque controller includes two FOC current control loops, one for each three-phase set [36]. Both loops include Proportional-Integral controllers (PI), decoupling feed-forward terms (19) and (20), derived from (5), and an anti-windup scheme.

$$ff_d = R_s i^*_d - \omega_e L_q i^*_q - \omega_e M_q i^*_q, \tag{19}$$

$$ff_q = R_s i^*_q + \omega_e L_d i^*_d + \omega_e \psi_{PM} + \omega_e M_d i^*_d. \tag{20}$$

The voltage references provided by the regulators are transformed from the $d-q$ reference frame into the respective three-phase values. Finally, the PWM module synthesizes the firing pulses, where a min-max type zero sequence injection block is included for the duty-cycle calculation to maximize the linear range of the output voltage [37].

It should be noted that in the adopted symmetrical IPMSM, the windings of both three-phase sets are overlapped, thus sharing the same stator slots. Therefore, the two sets present a mutual leakage inductance, highly coupling the two windings at PWM frequency. If a standard PWM technique is adopted, this results in an extremely high current ripple, with the consequent additional loss, acoustic noise, and poor control performance [23], [38]. All these effects are strongly mitigated by phase-shifted or interleaved PWM [28], [39], [40]. In [41], [42], the mathematical expressions that allow calculating the optimal phase-shift between the carrier of each three-phase set of a six-phase machine are detailed. Here, a phase-shift of π radians is applied (Fig. 10).

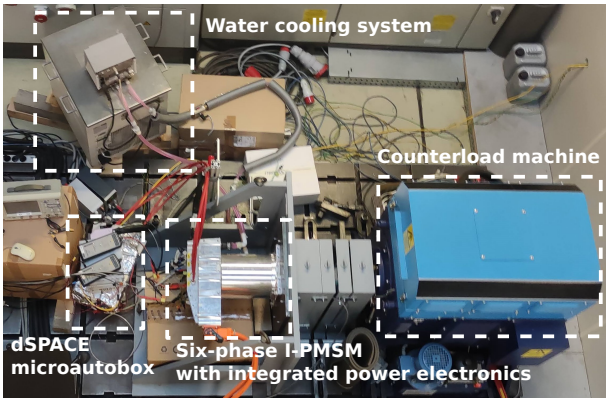

Figure 11: Experimental platform including the six-phase IPMSM.

Table I: Relevant nominal parameters of the dual three-phase drive prototype.

Parameter	Value	Units
Electric machine		
Pole-pair number (N_P)	3	-
d-axis nominal inductance (L_{dnom})	55.6	μH
q-axis nominal inductance (L_{qnom})	291.3	μH
Stator resistance (R_s)	8.8	$m\Omega$
PM nominal flux (ψ_{PM})	0.029	Wb
Nominal power (P_{nom})	70	kW
Nominal torque ($T_{em,nom}$)	80	Nm
Nominal mechanical speed ($w_{mech,nom}$)	8000	r/min
Maximum power (P_{max})	135	kW
Maximum torque ($T_{em,max}$)	170	Nm
Maximum mechanical speed ($w_{mech,max}$)	22000	r/min
Maximum current per phase (I_{max})	235	Arms
Power electronics		
dc-link capacitance	320	μF
Switching frequency (f_{sw})	24	kHz
Total dc-link voltage	480 to 800	V

IV. Experimental validation

A. Experimental platform description

Fig. 11 shows the experimental platform used initially to validate the proposed control approach. It includes a full-scale traction symmetrical dual three-phase IPMSM prototype within project FITGEN, which development was led by BRUSA Elektronik AG, coupled to a load machine through a torque transducer. The load machine is speed regulated, while the machine under test is torque regulated. The six-phase SiC inverter with cascaded dc-link capacitors is incorporated at the rear side of the machine housing. Table I summarizes the most relevant nominal parameters of the electric drive prototype. A dSPACE MicroAutoBox II Rapid Control Prototyping (RCP) platform (including an IBM PPC 750GL at 900 MHz and 16 parallel 16-bit ADC channels with a conversion rate of 1 Msps) has been used to implement the proposed control algorithm.

B. Current regulation, field weakening and voltage balancing

Several experimental tests have been carried out in order to validate the main parts of the controller, i.e., the current (torque) regulation loops, the voltage balancing algorithm, and the current setpoint generation block (MTPA and FW).

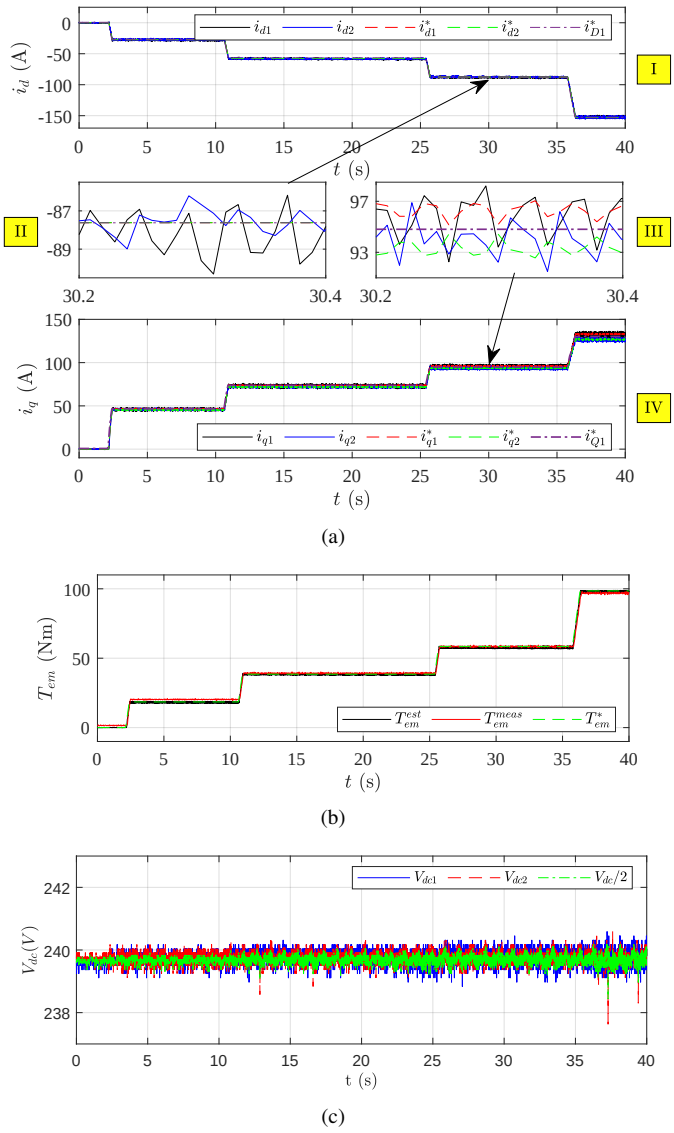

Figure 12: Experimental results obtained for various torque steps. (a) dq-axis currents, (b) electromagnetic torque, and (c) dc-link voltage balancing.

Fig. 12 shows the experimental results obtained when the machine rotates at 2500 rpm and various torque steps are applied. The dq currents of both three-phase winding sets are regulated to the MTPA reference values [Figs. 12(a)-I and -IV]. As a result, the measured (T_{em}^{meas}) and estimated (T_{em}^{est}) electromagnetic torque produced by the machine tracks the reference torque [Fig. 12(b)]. Slight differences between the setpoint and the torque measurement are caused by small inaccuracies in the drive model parameters. However, the torque estimated from current measurements tracks the reference more closely. Note that the reference torque slew rate is limited to 100 Nm/s (1250 Nm/s on wheel thanks to a gearbox) to ensure driver's and passenger's comfort.

The control action of the dc-voltage balancing algorithm is shown in detail in Fig. 12(a). As it can be seen from Fig. 12(a)-III, the balancing algorithm modifies the q-axis current references since the mean value of the references i_{q1}^* and i_{q2}^* are $\pm 1A$ away from the LUT reference i_{Q1}^*. In addition,

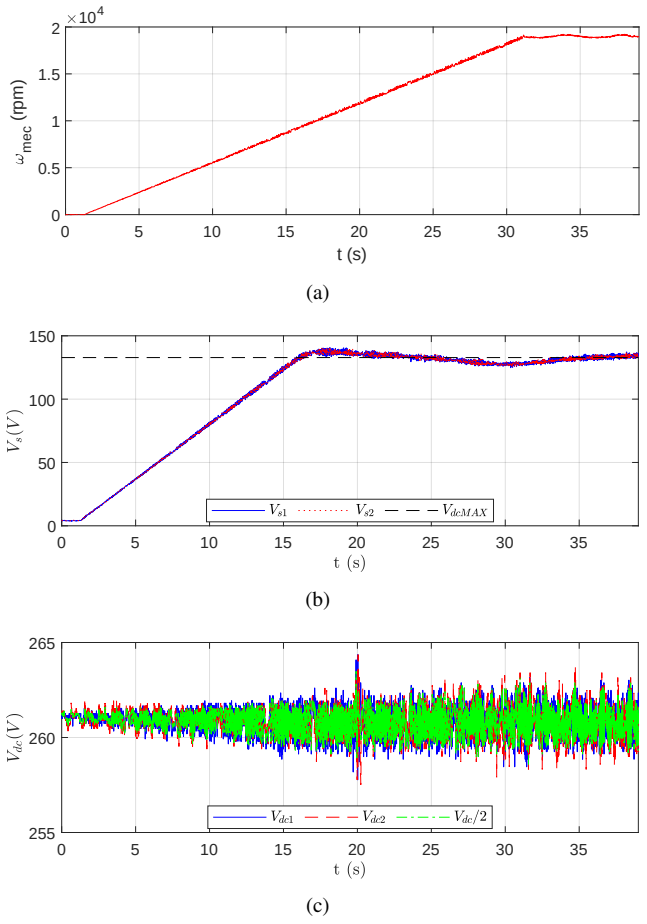

Figure 13: Experimental results obtained when accelerating the six-phase IPMSM up to 19000 rpm. (a) Mechanical speed, (b) stator voltages, and (c) dc-link voltage balancing.

i_{q1}^* and i_{q2}^* fluctuate themselves in steady state conditions with an amplitude of $\pm 1A$ (only 0.5 % of the maximum inverter current). In contrast, the d-axis currents references are unaltered during steady-state conditions [Fig. 12(a)-II]. The dynamics of the voltage balancing loop are fast enough to keep V_{dc1} and V_{dc2} around $V_{dc}/2$ during steady state and transients [Fig. 12(c)].

To validate the FW algorithm, including the VCT loop, the electric machine has been accelerated from standstill up to 19000 rpm [Fig. 13(a)] while a constant torque setpoint of 30 Nm is commanded. Thanks to the proposed field weakening approach, the two three-phase set stator voltages v_{s1} and v_{s2} are kept below the maximum voltage limit, $v_{dcMAX} = k_v V_{dc}/2\sqrt{3}$ during the whole test [Fig. 13(b)]. The dc-link voltage of each inverter unit is kept balanced thanks to the proposed voltage balancing algorithm [Fig. 13(c)]. These voltages would become unbalanced and jeopardize the integrity of the power system if the balancing algorithm were not active.

C. Interleaved PWM

The performance of the electric drive is tested under the application of a conventional carrier-based PWM scheme and later with the interleaved PWM pattern incorporated in this paper. Fig. 14 shows the phase currents obtained during early tests, where the *Double zero-sequence injection modulation technique* [43] is used with no phase shift. Fig. 14(b) shows the high undesired phase current components generated at the fundamental and third harmonic of the switching frequency (f_{sw}). Where f_e is the actual electric frequency. In contrast, Fig. 15 shows how the use of the interleaved PWM effectively eliminates the ripple in the phase currents. Apparent high-frequency electromagnetic noise is caused by the use of current probes having low disturbance rejection. Such fictitious high-

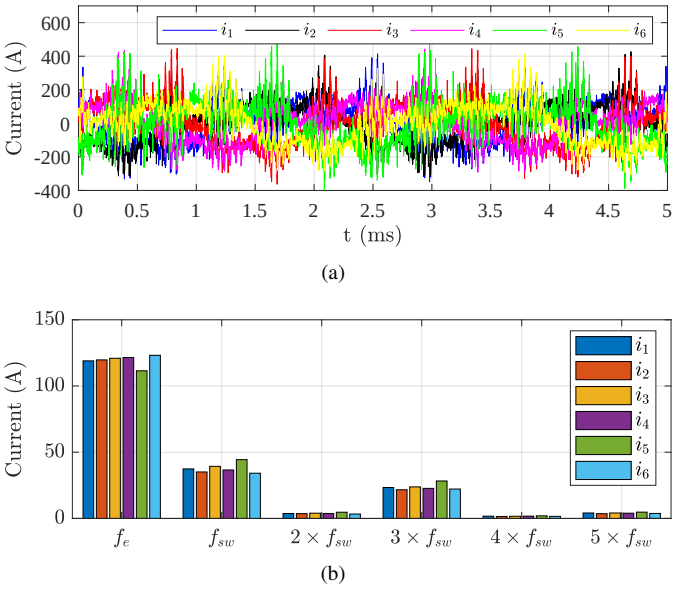

Figure 14: Phase currents with high ripple obtained without interleaving during early tests, when a 50 Nm torque is requested at 7800 rpm. (a) Phase currents and (b) frequency spectrum of phase currents.

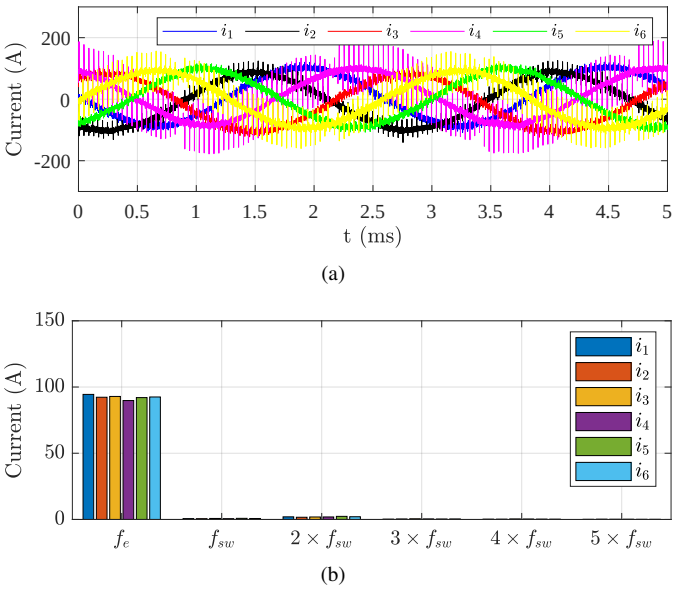

Figure 15: Phase currents with low ripple thanks to the interleaved PWM, when a 40 Nm torque is requested at 7800 rpm. (a) Phase currents and (b) frequency spectrum of phase currents.

Figure 16: Electric vehicle used to carry out the verification of the proposed control approach under standardized driving cycles.

frequency noise is not present in the real motor current.

D. Driving cycle results in real electric vehicle

Finally, the electric drive has been integrated and validated in a real electric vehicle under realistic driving and harsh environmental conditions within project FITGEN, led by Centro Ricerche FIAT SCPA (CRF). Tests have been carried out on-road and with the vehicle mounted over a dynamometer (Fig. 16). Fig. 17 shows the experimental results obtained when the vehicle is operated under a World Harmonized Light-duty Vehicle Test Procedure (WLTP) driving cycle. This cycle characterizes the speed and torque profiles [Fig. 17(a)] for which the machine should operate in a typical urban and extra-urban route.

As shown in Fig. 17(a), the generated electromagnetic torque tracks the reference one satisfactorily. The performance of current regulators is shown in Fig. 17(b), where i_{d1} and i_{q1} currents of the first winding set track their references. Equivalent results are obtained for the second winding set. These results validate both the setpoint generation approach and the convenience of the used vector representation.

What is more, the drive operates with a variable dc-link voltage produced by the dc/dc converter. The voltages of the cascaded dc-link capacitors are kept balanced for the whole trip thanks to the proposed balancing scheme [Fig. 17(c)]. In general, a dc-link voltage ripple of approximately 3 V is obtained, although higher deviations are produced while the vehicle is at standstill (at zero speed and with zero torque command), as the balancing algorithm is disabled to avoid any torque production. Minor variations up to ± 5 V, with respect to the reference voltage, are observed, but the action of the balancing algorithm leads to a fast equilibration of both voltages once the machine produces torque again.

Besides the WLTP, three other driving cycles were successfully tested and validated. Fig. 18 maps the cycles' operating points and compares them to the rated torque curve. Where RWC1 and RWC2, Real World driving Cycle 1 and 2, are two urban routes in the Turin area. The last cycle is the US06 Supplemental Federal Test Procedure (SFTP). In this figure, the ratio between vehicle and machine rotation speeds is shown.

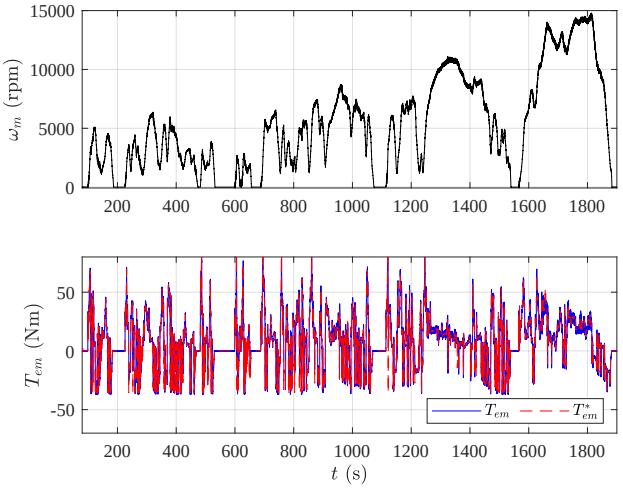

(a)

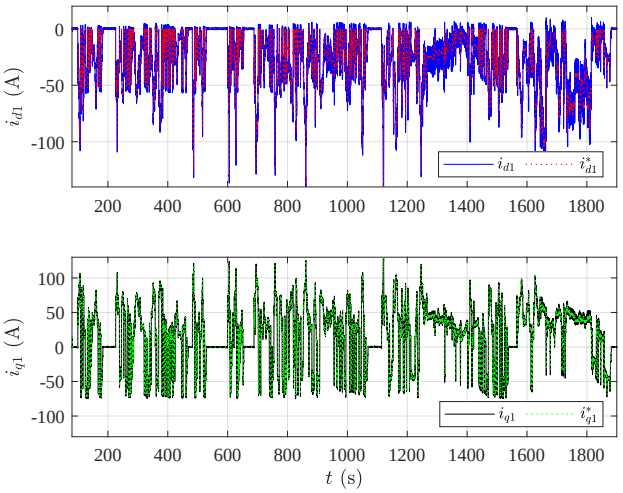

(b)

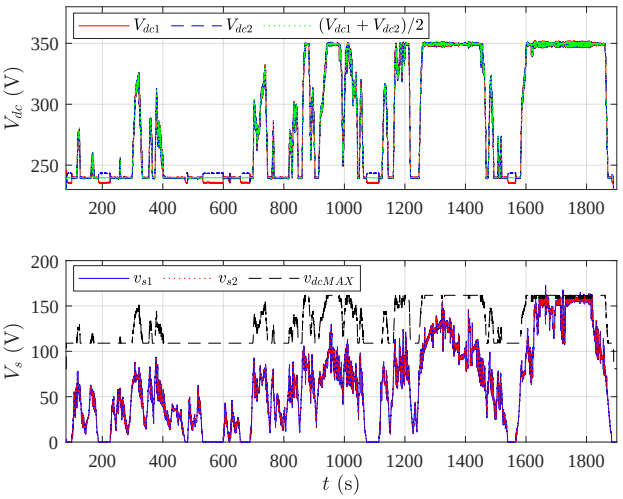

(c)

Figure 17: Experimental results obtained for the WLTP driving cycle with the electric vehicle under test. (a) Mechanical speed and Torque vs. reference torque, (b) dq-axis current in the first three-phase winding set, and (c) dc-link balancing and stator voltage regulation.

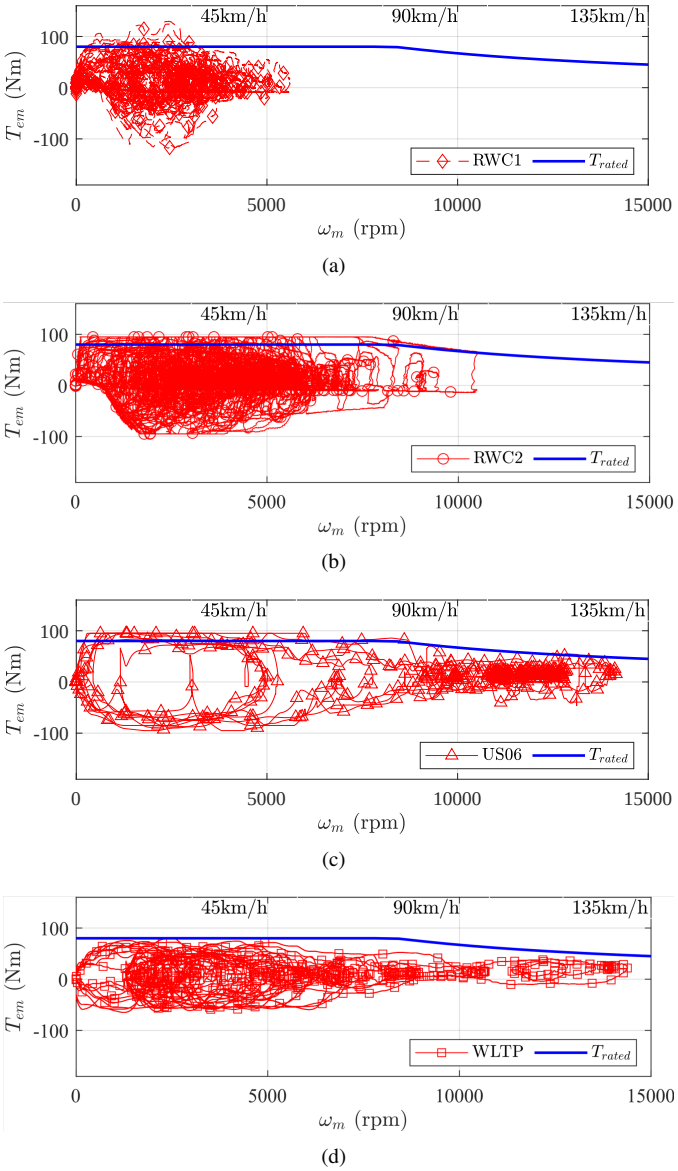

Figure 18: Operating points map of the tested driving cycles: (a) RWC1, (b) RWC2, (c) US06 and (d) WLTP.

V. Conclusion

In this work, a novel control approach to regulate the torque production of a symmetrical six-phase IPMSM drive with a cascaded dc-link configuration has been proposed, developed, and experimentally validated in a full-scale traction drive. This approach conveniently makes use of the different vector representations and meets the automotive requirements: torque control accuracy in the full speed range, safe operation, and low computational burden. The feasibility of this type of solution for the automotive scenario has also been initially demonstrated at TRL6 using several driving cycles. Furthermore, a TRL7 validation of the drive under test in a commercial EV platform has been completed.

To the best of authors' knowledge, it is the first time that this type of cascaded dc-link configuration has been successfully applied for EV applications at full-scale level. Finally, it is important to point out that although this control solution has been originally proposed for a symmetrical dual three-phase machine, the developed control can be extended to asymmetrical dual three-phase machines or even to multiple three-phase motors by adapting the transformation matrix.

Acknowledgment

The authors are grateful to the European Commission for supporting the present work performed within the EU H2020 project FITGEN (Grant Agreement 824335). The authors are grateful to the Government of the Basque Country for supporting the present work performed within the fund for research groups of the Basque University (IT1440-22) and the research program ELKARTEK as the projects PROH2BIO (KK-2022/00051) and VEGAN (KK-2021/00044). The authors are grateful to the MCIN/AEI/10.13039/501100011033 for the support to the present work performed within the project PID2020-115126RB-I00.

The research has been conducted with the support of AIT Austrian Institute of Technology GmbH, Centro Ricerche Fiat SCPA, Tecnalia Research & Innovation, Brusa Elektronik AG, Politecnico di Torino, STMicroelectronics SRL, GKN Driveline International GmbH, and Vrije Universiteit Brussel.

References

[1] A. Sierra-Gonzalez, P. Pescetto, E. Trancho, E. Ibarra, G. Pellegrino, and F. Alvarez-Gonzalez, "Control of dual three-phase IPMSM drive with cascaded DC-link capacitors for third generation EV," in *Proc. of the IEEE Energy Conversion Congress and Exposition (ECCE)*, 2021, pp. 4822–4829.

[2] D. Ivanova, J. Barrett, D. Wiedenhofer, B. Macura, M. Callagham, and F. Creutzig, "Quantifying the potential for climate change mitigation of consumption options," *Environmental Research Letters*, vol. 15, no. 9, pp. 1–19, 2020.

[3] I. López, E. Ibarra, A. Matallana, J. Andreu, and I. Kortabarria, "Next generation electric drives for HEV/EV propulsion systems: Technology, trends and challenges," *Renewable and Sustainable Energy Reviews*, vol. 114(109336), pp. 1–23, 2019.

[4] European Commission, Joint Research Centre, A. Tsakalidis, K. Gkoumas, M. Balen, F. Marques dos Santos, M. Grosso, A. Ortega Hortelano, and F. Pekár, *Research and innovation in transport electrification in Europe : an assessment based on the Transport Research and Innovation Monitoring and Information System (TRIMIS)*. Publications Office, 2020.

[5] A. Mohammadpour and L. Parsa, "Global fault-tolerant control technique for multiphase permanent-magnet machines," *IEEE Transactions on Industry Applications*, vol. 51, no. 1, pp. 178–186, 2015.

[6] A. G. Yepes, O. Lopez, I. Gonzalez-Prieto, M. J. Duran, and J. Doval-Gandoy, "A comprehensive survey on fault tolerance in multiphase AC drives, part 1: General overview considering multiple fault types," *Machines*, vol. 10, no. 3, 2022.

[7] A. Salem and M. Narimani, "A review on multiphase drives for automotive traction applications," *IEEE Transactions on Transportation Electrification*, vol. 5, no. 4, pp. 1329–1348, 2019.

[8] A. Matallana, E. Ibarra, I. López, J. Andreu, J. Garate, X. Jorda, and J. Rebollo, "Power module electronics in HEV/EV applications: New trends in widebandgap semiconductor technologies," *Renewable and Sustainable Energy Reviews*, vol. 113(109264), pp. 1–33, 2019.

[9] M. Martino, P. Pescetto, and G. Pellegrino, "Advanced functionally integrated E-Axle for A-Segment electric vehicles," in *Proc. of the AEIT International Conference of Electrical and Electronic Technologies for Automotive*, 2020, pp. 1–6.

[10] European Union funded Project. (2019) FITGEN, Functionally integrated e-axle ready for mass market third generation electric vehicles. [Online]. Available: https://fitgen-project.eu/

[11] P. Pescetto, A. Sierra-Gonzalez, E. Trancho, and G. Pellegrino, "Variable DC-link control strategy for maximum efficiency of traction motor drives," in *Proc. of the IEEE Energy Conversion Congress and Exposition (ECCE)*, 2021, pp. 4815–4821.

[12] J. O. Estima and A. J. Marques Cardoso, "Efficiency Analysis of Drive Train Topologies Applied to Electric/Hybrid Vehicles," *IEEE Transactions on Vehicular Technology*, vol. 61, no. 3, pp. 1021–1031, 2012.

[13] K. K. Prabhakar, M. Ramesh, A. Dalal, C. U. Reddy, A. K. Singh, and P. Kumar, "Efficiency investigation for electric vehicle powertrain with variable DC-link bus voltage," in *IECON 2016 - 42nd Annual Conference of the IEEE Industrial Electronics Society*, 2016, pp. 1796–1801.

[14] T. Schoenen, M. S. Kunter, M. D. Hennen, and R. W. De Doncker, "Advantages of a variable DC-link voltage by using a DC-DC converter in hybrid-electric vehicles," in *2010 IEEE Vehicle Power and Propulsion Conference*, 2010, pp. 1–5.

[15] H. Chen, H. Kim, R. Erickson, and D. Maksimović, "Electrified Automotive Powertrain Architecture Using Composite DC–DC Converters," *IEEE Transactions on Power Electronics*, vol. 32, no. 1, pp. 98–116, 2017.

[16] J. Kacetl, J. Fang, T. Kacetl, N. Tashakor, and S. Goetz, "Design and Analysis of Modular Multilevel Reconfigurable Battery Converters for Variable Bus Voltage Powertrains," *IEEE Transactions on Power Electronics*, vol. 38, no. 1, pp. 130–142, 2023.

[17] K. Toshiyuki, H. Na, K. Eritate, N. Takamatsu, M. Okamura, and M. Taki, "Bidirectional DC-DC converter utilizing new loss reduction techniques for HV/PHV," in *2020 IEEE Applied Power Electronics Conference and Exposition (APEC)*, 2020, pp. 3484–3488.

[18] K. K. Prabhakar, U. R. Chinthakunta, A. K. Singh, and P. Kumar, "Efficiency and performance analysis of DTC-based IM drivetrain using variable DC-link voltage for electric vehicle applications," *IET Electrical Systems in Transportation*, vol. 8, no. 3, pp. 205–214, 2018.

[19] J. Wang, B. Wang, L. Zhang, J. Wang, N. Shchurov, and B. Malozyomov, "Review of bidirectional DC–DC converter topologies for hybrid energy storage system of new energy vehicles," *Green Energy and Intelligent Transportation*, vol. 1, no. 2, pp. 1–18, 2022.

[20] S. Morimoto, Y. Takeda, T. Hirasa, and K. Taniguchi, "Expansion of operating limits for permanent magnet motor by current vector control considering inverter capacity," *IEEE Transactions on Industry Applications*, vol. 26, no. 5, pp. 866–871, 1990.

[21] Z. Yu, C. Gan, K. Ni, R. Qu, and W. Kong, "Dual three-phase flux-modulated switched reluctance motor drive with maximum torque per ampere strategy," *IEEE Transactions on Industry Applications*, vol. 57, no. 6, pp. 5806–5817, 2021.

[22] E. Trancho, E. Ibarra, A. Arias, I. Kortabarria, J. Jurgens, L. Marengo, and A. Fricasse, "PM-assisted synchronous reluctance machine flux weakening control for EV and HEV applications," *IEEE Transactions on Industrial Electronics*, vol. 65, no. 4, pp. 2986–2995, 2018.

[23] H. S. Che, E. Levi, M. Jones, M. J. Duran, W.-P. Hew, and N. A. Rahim, "Operation of a six-phase induction machine using series-connected machine-side converters," *IEEE Transactions on Industrial Electronics*, vol. 61, no. 1, pp. 164–176, 2014.

[24] S. M. Dabour, A. S. Abdel-Khalik, S. Ahmed, and A. M. Massoud, "A new dual series-connected nine-switch converter topology for a twelve-phase induction machine wind energy system," in *Proc. of the 11th IEEE International Conference on Compatibility, Power Electronics and Power Engineering (CPE-POWERENG)*, 2017, pp. 139–144.

[25] Z. Xiang-Jun, Y. Yongbing, Z. Hongtao, L. Ying, F. Luguang, and Y. Xu, "Modelling and control of a multi-phase permanent magnet synchronous generator and efficient hybrid 3L-converters for large direct-drive wind turbines," *IET Electric Power Applications*, vol. 6, pp. 322–331(9), 2012.

[26] S. S. Gjerde, P. K. Olsen, K. Ljøkelsøy, and T. M. Undeland, "Control and fault handling in a modular series-connected converter for a transformerless 100 kV low-weight offshore wind turbine," *IEEE Transactions on Industry Applications*, vol. 50, no. 2, pp. 1094–1105, 2014.

[27] M. Nikouie, O. Wallmark, L. Jin, L. Harnefors, and H.-P. Nee, "DC-link stability analysis and controller design for the stacked polyphase bridges converter," *IEEE Transactions on Power Electronics*, vol. 32, no. 2, pp. 1666–1674, 2017.

[28] Y. Han, "Design, modeling, and control of multilevel converter motor drive with modular design and split winding machine," in *2014 IEEE 15th Workshop on Control and Modeling for Power Electronics (COMPEL)*, 2014, pp. 1–10.

[29] J. Karttunen, S. Kallio, P. Peltoniemi, P. Silventoinen, and O. Pyrhonen, "Dual three-phase permanent magnet synchronous machine supplied by two independent voltage source inverters," in *Proc. of the International Symposium on Power Electronics Power Electronics, Electrical Drives, Automation and Motion (SPEEDAM)*, 2012, pp. 741–747.

[30] J. Kolar and S. Round, "Analytical calculation of the RMS current stress on the DC-link capacitor of voltage-PWM converter systems," *IEE Proceedings - Electric Power Applications*, vol. 153, pp. 535–543(8), 2006.

[31] M. Schiedermeier, F. Schlamp, C. Rettner, and M. März, "Analytical calculation of the RMS value and the spectrum of the DC-link current of a dual-inverter," *IEEE Transactions on Power Electronics*, vol. 37, no. 1, pp. 782–794, 2022.

[32] M. Ganchev, C. Kral, and T. Wolbank, "Sensorless rotor temperature estimation of permanent magnet synchronous motor under load conditions," in *Proc. of the Annual Conference of the IEEE Industrial Electronics Society (IECON)*, 2012, pp. 1989–1994.

[33] E. Armando, R. Bojoi, P. Guglielmi, G. Pellegrino, and M. Pastorelli, "Experimental identification of the magnetic model of synchronous machines," *IEEE Transactions on Industry Applications*, vol. 49, no. 5, pp. 2116–2125, 2013.

[34] P. Pescetto and G. Pellegrino, "Sensorless magnetic model and PM flux identification of synchronous drives at standstill," in *Proc. of the IEEE International Symposium on Sensorless Control for Electrical Drives (SLED)*, 2017, pp. 79–84.

[35] S. A. Odhano, P. Pescetto, H. A. A. Awan, M. Hinkkanen, G. Pellegrino, and R. Bojoi, "Parameter identification and self-commissioning in AC motor drives: A technology status review," *IEEE Transactions on Power Electronics*, vol. 34, no. 4, pp. 3603–3614, 2019.

[36] Y. Hu, Z. Q. Zhu, and M. Odavic, "Comparison of two-individual current control and vector space decomposition control for dual three-phase PMSM," *IEEE Transactions on Industry Applications*, vol. 53, no. 5, pp. 4483–4492, 2017.

[37] V. Blasko, "Analysis of a hybrid PWM based on modified space-vector and triangle-comparison methods," *IEEE Transactions on Industry Applications*, vol. 33, no. 3, pp. 756–764, 1997.

[38] H. Zhang, O. Wallmark, M. Leksell, S. Norrga, M. N. Harnefors, and L. Jin, "Machine design considerations for an MHF/SPB-converter based electric drive," in *Proc. of the 40th Annual Conference of the IEEE Industrial Electronics Society (IECON)*, 2014, pp. 3849–3854.

[39] Y. Huang, Y. Xu, W. Zhang, and J. Zou, "PWM frequency noise cancellation in two-segment three-phase motor using parallel interleaved inverters," *IEEE Transactions on Power Electronics*, vol. 34, no. 3, pp. 2515–2525, 2019.

[40] K. Cui, C. Wang, M. Zhou, and S. Sun, "Comprehensive investigation of space-vector PWM including novel switching sequences for dual three-phase motor drives," *IEEE Transactions on Transportation Electrification*, pp. 1–1, 2022.

[41] Y. Miyama, M. Ishizuka, H. Kometani, and K. Akatsu, "Vibration reduction by applying carrier phase-shift PWM on dual three-phase windings permanent-magnet synchronous motor," in *Proc. of the IEEE International Electric Machines and Drives Conference (IEMDC)*, 2017, pp. 1–6.

[42] Y. Miyama and K. Akatsu, "Dual three-phase-winding permanent-magnet synchronous motors: An investigation of the optimal carrier phase-shift angle," *IEEE Industry Applications Magazine*, vol. 27, no. 6, pp. 12–21, 2021.

[43] R. Bojoi, A. Tenconi, F. Profumo, G. Griva, and D. Martinello, "Complete analysis and comparative study of digital modulation techniques for dual three-phase AC motor drives," in *Proc.of the 33rd Annual IEEE Power Electronics Specialists Conference (Cat. No.02CH37289)*, vol. 2, 2002, pp. 851–857.

Andres Sierra-Gonzalez received his Bachelor's in Electronic and Electrical Engineering and first M.Eng. degree in 2008 and 2015 from Andes University, Bogotá, Colombia. Then, he received his second M.Eng. degree from the University of the Basque Country, San Sebastian, Spain, in 2017. He is pursuing a Ph.D. in Electronics and Telecommunication at the University of the Basque Country. He worked as an Electronics Engineer in the mining and energy industry from 2009 to 2013. Next, he was a research assistant at Andes University from 2014 to 2016. Then, he worked as a researcher in the Energy Management division of IK4-IKERLAN in 2017. Since 2018 he has worked as Control Systems Researcher applied to electromobility at Tecnalia Research & Innovation (Spain). Besides, Mr. Sierra was co-recipient of the Best Paper Award for the IEEE Vehicular Power and Propulsion Conference (VPPC) in 2017.

Paolo Pescetto (S'16 – M'19) received the B.Sc. and M.Sc. degrees with full grade and honors from Politecnico di Torino, Turin, Italy, in 2013 and 2015. Since 2015 he worked in the same institution toward the Ph.D. degree obtained "Cum Laudem" in 2019. Since the fall of 2019, he is working as researcher and tenure-track lecturer in the Energy Department of Politecnico di Torino. He is a member of the Power Electronics Innovation Center (PEIC) of Politecnico di Torino. In 2014 he was an Erasmus Student at the Norwegian University of Science and Technology, Trondheim. He authored or co-authored 10+ IEEE journal papers. His main research interests include synchronous motor drives, sensorless control, self-commissioning techniques, and integrated battery chargers for EVs. Dr. Pescetto received five IEEE Paper Awards and two IEEE Ph.D. thesis awards.

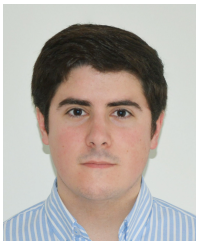

Fernando Alvarez-Gonzalez received a B.Eng. degree in electronic engineering and M.Eng. degree in electrical and electronic engineering from the University of Overdo, Asturias, Spain, in 2012 and 2014, respectively, including a three-month research stay at the University of Nottingham PEMC group, Nottingham, U.K., in 2014. He received a Ph.D. in electronic and electrical engineering from The University of Sheffield, Sheffield, U.K., in 2019. From 2018 to 2020, he was a Postdoctoral Research Associate at The University of Sheffield's EMD group. Since 2020 he has been a researcher with Tecnalia Research & Innovation, where he works on sustainable mobility. His current research interests include modeling, control, fault detection, and condition monitoring of electric machines and power electronics.

Borja Heriz received his Electronic & Control Engineering degree in 2008 and his postgraduate in Control Systems and Industrial Automation Engineering in 2011, both from the University of the Basque Country. Since 2010 he has worked at Tecnalia Research & Innovation as hybrid powertrain control engineer.

Elena Trancho received the M.Sc. degree in Automatic and Electronic Engineering from the University of Deusto, Spain, in 2011, the M.SC degree in Electrical Engineering from the Institut Nationale Politechnique, Toulouse, France, in 2012, and the Ph.D. in Automatic and Electronic Engineering for the University of the Basque Country in 2018. From 2012 to 2014, she worked at Akka Technologies, France, as an advanced flight control researcher. Since 2014 she has worked at Tecnalia Research & Innovation (Spain) as an advanced drives control researcher. Her research interests include electric and hybrid vehicles, variable-speed drives, advanced control strategies, and sensorless techniques.

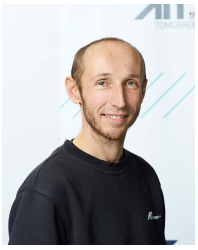

Hannes Lacher received his Electronic Engineering degree in 2003 at the Fachhochschule Technikum Wien (Advanced Technical College). From 2004 to 2005, he worked as a technical employee of Toyota Frey Ges.m.b.H. Austria, where he was responsible for vehicle reparation and warranty handling. Since 2005 he has been a scientific employee at the AIT, Austrian Institute of Technology in the Mobility Department - Business Unit: Electric Vehicle Technologies.

Edorta Ibarra received the first M.Sc. degree in electronic engineering from the University of the Basque Country, Bilbao, Spain, in 2004, the second M.Sc. degree in electronic physics from the University of Cantabria, Santander, Spain, in 2005, and the Ph.D. degree from the University of the Basque Country, in 2011. From 2007 to 2014, he was with the Applied Electronic Research Group at the University of the Basque Country. From 2014 to 2016, he was with Tecnalia Research & Innovation, Derio, Spain. Since 2016, he has been an Assistant Professor in the Department of Electronic Technology, University of the Basque Country. His current research interests include power electronics for electromobility and particle accelerators.

Gianmario Pellegrino (Fellow, IEEE) received the M.Sc. and Ph.D. degrees in electrical engineering from Politecnico di Torino, Turin, Italy, in 1998 and 2002, respectively. He is a Full Professor of power converters, electrical machines and drives with Politecnico di Torino. He was a visiting scholar at Aalborg University, Denmark, in 2002, at the University of Nottingham in the U.K. in 2010–2011, and at the University of Wisconsin–Madison, USA, in 2013. He is engaged in several funded and commercial research projects with the industry in the fields of electric motor design and e-drives control and is a founding author of the open-source project SyR-e for the design of electric motors and drives. He coauthored 190 Scopus-indexed technical publications, including 60 IEEE Journal articles, two books, and eight patents. Dr. Pellegrino is an Associate Editor for the IEEE Transactions on Industry Applications. He is the recipient of the 8th Grand Nagamori Award and nine best paper awards. He is a founding member of the Power Electronics Interdepartmental Center (PEIC), Politecnico di Torino, a member of the Advisory Board of PCIM Europe, and the Advisor to the Rector of Politecnico di Torino for the implementation of interdepartmental centers of Politecnico di Torino.